SAND2016-4201J

Experimental Validation Benchmark Data for CFD of Transient Convection from Forced to Natural with Flow Reversal on a Vertical Flat Plate

Blake W. Lance
Advanced Nuclear Concepts
Sandia National Laboratories
Albuquerque, NM 87185
blance@sandia.gov

Barton L. Smith
Professor, Fellow of ASME
Mechanical & Aerospace Engineering
Utah State University
Logan, UT 84322
barton.smith@usu.edu

Transient convection has been investigated experimentally for the purpose of providing Computational Fluid Dynamics (CFD) validation benchmark data. A specialized facility for validation benchmark experiments called the Rotatable Buoyancy Tunnel was used to acquire thermal and velocity measurements of flow over a smooth, vertical heated plate. The initial condition was forced convection downward with subsequent transition to mixed convection, ending with natural convection upward after a flow reversal. Data acquisition through the transient was repeated for ensemble-averaged results. With simple flow geometry, validation data were acquired at the benchmark level. All boundary conditions (BCs) were measured and their uncertainties quantified. Temperature profiles on all four walls and the inlet were measured, as well as as-built test section geometry. Inlet velocity profiles and turbulence levels were quantified using Particle Image Velocimetry. System Response Quantities (SRQs) were measured for comparison with CFD outputs and include velocity profiles, wall heat flux, and wall shear stress. Extra effort was invested in documenting and preserving the validation data. Details about the experimental facility, instrumentation, experimental procedure, materials, BCs, and SRQs are made available through this paper. The latter two are available for download and the other details are included in this work.

Nomenclature

$B_{\bar{x}}$ Bias uncertainty of general mean quantity $\bar{x}$
D Experimental data or pipe diameter
dt Time delay of Particle Image Velocimetry image pairs
E Validation comparison error
g Acceleration due to gravity
Gr_x Local Grashof number
N Number of samples
N_m Number of transient repeats in ensemble average
q'' Wall heat flux
Re_1 Initial Reynolds number
Re_2 Final Reynolds number
Re_x Local Reynolds number
Ri_x Local Richardson number
S Simulation result
S_x Standard deviation of quantity x
$S_{\bar{x}}$ Random uncertainty of mean quantity $\bar{x}$
t Time or thickness
t_{95} Confidence level coefficient at 95%
T_s Temperature of wall
T_∞ Temperature of free-stream
U_D Validation data uncertainty
$U_{\bar{x}}$ Total uncertainty of mean quantity $\bar{x}$
U_{input} Simulation uncertainty due to input uncertainty
U_{num} Numeric uncertainty
U_{val} Validation uncertainty
$\bar{u}$ Ensemble-average streamwise (x) velocity
$\bar{u}_{\mathrm{bulk}}$ Ensemble-average streamwise (x) bulk velocity
u_m Scalar streamwise raw velocity
u_τ Friction velocity
$\overline{u'u'}$ Ensemble-average Reynolds normal stress
$\overline{u'v'}$ Ensemble-average Reynolds shear stress
$\bar{v}$ Ensemble-average heated wall-normal (y) velocity
v_m Scalar wall-normal raw velocity
$\overline{v'v'}$ Ensemble-average Reynolds normal stress
$\bar{w}$ Ensemble-average transverse (z) velocity
$\overline{w'w'}$ Ensemble-average Reynolds normal stress

x Streamwise direction
$\bar{x}$ General ensemble-average variable
y Heated wall-normal direction
y^+ Nondimensional heated wall-normal direction
z Transverse direction
α Dimensionless ramp rate parameter
β Volumetric thermal coefficient of expansion
γ Dimensionless ramp rate parameter
μ Dynamic viscosity
ν Kinematic viscosity
ρ Density
ϕ Phase
τ_s Wall shear stress

1 Introduction

The purpose of this work is to provide validation benchmark data for three-dimensional Computational Fluid Dynamics (CFD) models. Model validation will be discussed as well as the physical phenomenon of mixed convection. The following sections describe the experimental facility, the associated instrumentation, the boundary conditions (BCs), the fluid and material properties, the test conditions, and the System Response Quantities (SRQs). This content follows the Validation Experiment Completeness table of Oberkampf and Smith [1] to guide description of validation experiments. This guidance ensures that important details are included with a high level of completeness. This work is a continuation of Harris *et al.* [2] and Lance *et al.* [3], which covered steady forced and mixed convection using similar methods and facilities.

All data will be presented in table format for direct use in validating models. The provided data include the BCs and SRQs shown in Table 1. The included BCs should provide modelers with all required information, avoiding assumptions on model inputs and reducing model form uncertainty [4]. The SRQ data are provided to modelers for direct comparison with model outputs. The experimental uncertainties of all provided data from bias and random sources are also provided and quantified at the 95% confidence level. Validation comparison errors can be calculated with the nominal data. Validation uncertainty can be calculated from the uncertainty of the nominal data [5].

Table 1. The available experimental data presented in this work separated into BC and SRQ types. All data except As-Built Geometry and Atmospheric Conditions are ensemble-averaged.

BCs	SRQs
As-Built Geometry	Velocity Profiles
Wall Temperatures	Reynolds Stress Profiles
Inlet Temperature	Wall Heat Flux
Inlet Velocity	Wall Shear
Atmospheric Conditions	

These data files are accessible in an online database in the Digital Commons of Utah State University's Library. The page dedicated to the data in this work is found at digitalcommons.usu.edu/engineering_datasets/2/. Links to specific files are included in this work with specific file names for the data type (BC or SRQ) and measured quantity. Generally, data are in table format as csv files. In addition to specific file links, all the files may be downloaded in the zipped file Files.zip.

1.1 Computational Fluid Dynamics Validation

To understand the need for experiments expressly aimed at providing validation benchmark data, one must first understand the different aims of validation and discovery experiments. Discovery experiments, where new physical phenomena are measured and analyzed, are common in research. Validation experiments do not necessarily measure new phenomena, but focus more on boundary and inflow conditions than discovery experiments, since validation experiments must capture all model inputs. In most cases, legacy experimental data from discovery experiments are not suitable for use in validation.

The purpose of validation experiments is to provide the information required to quantify the uncertainty of a mathematical model. This uncertainty helps decision makers quantify model credibility. The ASME V&V 20 Standard [5] outlines an approach to estimate the validation comparison error and the validation uncertainty. The validation comparison error E is the difference between the simulation result S and the validation experiment result D as

$$E = S - D. \tag{1}$$

Calculating the validation uncertainty estimates the confidence interval of the error by considering both numerical and experimental uncertainty. Validation uncertainty is calculated as

$$U_{\text{val}} = \sqrt{U_{\text{num}}^2 + U_{\text{input}}^2 + U_D^2}, \tag{2}$$

where U_{num} is the numerical uncertainty, U_{input} is the simulation uncertainty due to input uncertainty, and U_D is the experimental data uncertainty. Equation 2 can be used when the validation variable is directly measured and the terms of the equation are independent but requires further development when the validation variable is not directly measured. The numerical uncertainty is estimated from solution verification with sources such as iterative and discretization uncertainty. The latter two uncertainties come from the validation benchmark data. The uncertainty in the simulation from the measured BCs used for model inputs is U_{input}. The uncertainty of SRQs—experimental data used to compare system outputs—is U_D. If $|E| >> U_{\text{val}}$, one can conclude model error remains. However, if $|E| \leq U_{\text{val}}$ and U_{val} is acceptably small for the intended use of the model, the validation comparison error may be satisfactory. These general equations

show validation data and their uncertainties are required to assess model accuracy via model validation.

Unintrusive measurement techniques are important in validation experiments because probes introduce unknown uncertainties to the data. These uncertainties can only be mitigated by including the probe in the CFD model, often increasing the model cost considerably.

It is useful to consider several tiers of detail in validation experiments [6], such as the four shown in Fig. 1. This work is considered a Benchmark Case that is second in simplicity to Unit Problems. The Benchmark Case, also called Separate Effects Testing, requires that all model inputs and most model outputs are measured and that experimental uncertainty is included. In this tier there is generally some level of multi-physics interaction, such as coupled fluid momentum and heat transfer, that prevents the current work from being considered a Unit Problem. On the other hand, the non-prototypical geometry used in this work keeps it from being a Subsystem Case.

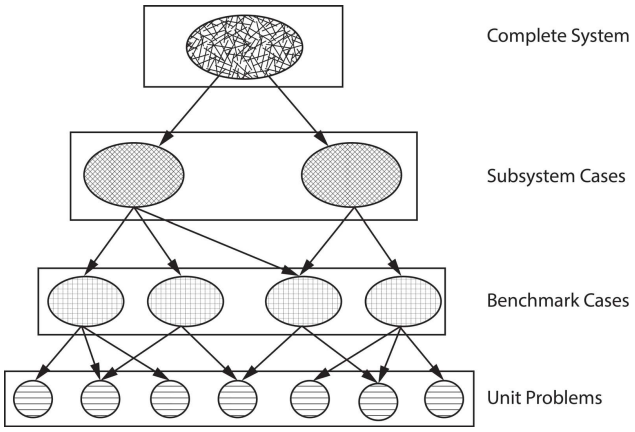

Fig. 1. The Validation Hierarchy, after [6]

In considering the design of validation benchmark experiments, SRQs should be measured from a wide range and high difficulty in the difficulty spectrum, as shown in Fig. 2. Comparing simulation results with experimental data from a wide range on the spectrum increases validation confidence. For example, integral quantities, such as fluid mass flow rate, generally have low experimental noise and random errors. Derivative quantities like fluid shear are more sensitive to non-ideal conditions. If a model and data are in good agreement at a high level, it is likely that good agreement will be observed in lower levels. However, agreement at lower levels does not imply agreement at higher levels [4].

1.2 Transient Flows

Some studies of non-periodic transient flow have been performed, but as He & Jackson note, technology has allowed for comprehensive measurements of ensemble-averaged transient experiments only recently [7]. This review covers adiabatic and convective ramp-type flow transients. Most of the first experiments measured either temperature of tube walls or velocity, but not both. A common observation was that accelerating flow suppresses turbulence while decelerating flow augments it, consistent with findings in the oscillating flow literature [8].

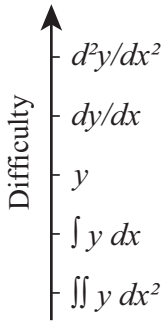

Fig. 2. System Response Quantity Difficulty Spectrum for arbitrary variables x and y, after [4]

The first known work by Koshkin *et al.* was published in 1970 for turbulent air flow. This study reported measurements during a change in electrical power and different flow transients, measuring and reporting temperature [9]. Two similar studies were published in the 1970s and used electrochemical techniques with probes to measure velocity profiles inside a tube from a step change in flow rate [10, 11].

Rouai [12] performed heat transfer experiments on ramp-up and ramp-down transients as well as periodic pulsating flow with a non-zero time mean. Water was heated by passing an alternating electrical current through a stainless steel tube. Temperature measurements were made by 24 thermocouples (TCs) welded to this tube. Flow transients were prescribed by using a constant head tank and varying the flow through the test section by a valve. Wall heat flux remained constant and changes in wall temperature were measured. The observed Nusselt number departed more from the psuedo-steady values for faster transients and for decelerating flows, likely from the augmentation of turbulence.

Jackson *et al.* performed a study on non-periodic ramping transients in a water tube [13]. This was similar to the study by Rouai, but measured local fluid temperature with a TC probe and improved computer control and data logging for greater repeatability and ensemble averaging. The TC probe was small enough to capture turbulent fluctuations. Jackson also found a suppression of turbulence, and consequently, wall heat transfer for accelerating ramps and augmentation during decelerating ramps. He also observed a peak in temperature fluctuations soon after the ramps began.

He & Jackson performed experiments in water using two-component LDA measurements in a clear, unheated tube. This non-intrusive velocity measurement was one of the first known to the authors for non-periodic flows. Ensemble averaged results were used for mean and turbulent quantities. The turbulent results were shown to deviate from psuedo-steady results for short transients. Several nondimensional parameters were recommended for ramp-type transients [7].

Barker and Williams [14] reported high speed measurements of an unsteady flow with heat transfer in air. They used a hot wire anemometer, a cold wire temperature probe, and a surface heat flux sensor to measure heat transfer coefficients for fully-developed turbulent pipe flow. Most results were for periodic flows, but some were presented for ramp-type transients with negligible buoyancy effects. The measurements were basic and provided data for conceptual model development.

In the previous studies, little coupling of velocity and thermal measurements was found for flow transients and buoyancy effects were negligible. Also, as these were discovery experiments, boundary conditions were not measured and provided as tabulated data, making the results of limited use for validation. The facility descriptions were very basic and little detail was provided about flow geometries. The current study contributes high fidelity measurements of a ramp-down transient suitable for validation studies with simultaneous, non-intrusive velocity and thermal measurements to provide validation benchmark data on simplified geometry for three-dimensional simulations. In contrast to previous studies, the geometry was rectangular and the flow was never fully developed.

The initial condition in this study was forced convection downward over a heated plate. Blower power was removed and the drum-type blower was allowed to coast to a stop, which took about 10 s. This resulted in ramp-down bulk velocity and subsequent flow reversal by natural convection. The bulk velocity at the test section inlet is shown in Fig. 3. The bulk velocity approaches zero at the end as there is both natural convection upward near the heated wall and recirculating flow downward far from the wall. There was measurable delay in the blower drive system, so $t = 0$ was defined as the last phase where the bulk velocity matched the steady state condition. Thus, the useful transient time spans $0 \leq t \leq 18.2$ s and data are presented in this range.

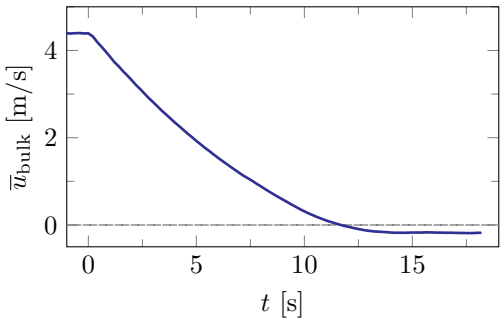

Fig. 3. Bulk velocity across the inlet at the spanwise center ($z = 0$) through time

1.3 Mixed Convection

The physics in this study include a flow transient with buoyancy effects, phenomena that have not, to our knowledge, been studied together. Convective flows with notable buoyancy effects are considered mixed or combined convection [15]. The Richardson number Ri is a measure of the relative magnitudes of buoyant and inertial forces and is defined by

$$\text{Ri}_x = \text{Gr}_x / \text{Re}_x^2 \tag{3}$$

where

$$\text{Gr}_x = g\beta(T_s - T_\infty)x^3/\nu^2 \tag{4}$$

and

$$\text{Re}_x = \overline{u}_{\text{bulk}} x/\nu. \tag{5}$$

In these, g is acceleration due to gravity, β is fluid thermal coefficient of expansion, $T_s = 130°\text{C}$ and $T_\infty = 20°\text{C}$ are surface and inlet fluid temperatures, respectively, x is local streamwise location, ν is fluid kinematic viscosity, and $\overline{u}_{\text{bulk}}$ is generally mean bulk velocity. In the current work $\overline{u}_{\text{bulk}}$ is the ensemble-average bulk velocity. Mixed convection is observed for buoyancy-aided flow when $0.3 < \text{Ri}_x < 16$ and for $0.3 < \text{Ri}_x$ for buoyancy-opposed flow [15].

Ensemble averaging was used throughout the current work to calculate average and fluctuating values where data within a given phase from all transient repeats were considered together. One way to understand this is with the ensemble average of a scalar streamwise velocity u_m that contains measured values for all repeats m and phases ϕ

$$\overline{u}(\phi) = \frac{1}{N_m} \sum_{m=1}^{N_m} u_m(\phi) \tag{6}$$

where $\overline{u}(\phi)$ is the ensemble-average and N_m is the number of repeats. The resulting $\overline{u}(\phi)$ is a function of ϕ, but the phase notation is omitted in the remainder of this work.

The Reynolds stresses were similarly ensemble-averaged for scalar velocities u_m and v_m as

$$\overline{u'v'}(\phi) = \frac{1}{N_m} \sum_{m=1}^{N_m} [u_m(\phi) - \overline{u}(\phi)]\,[v_m(\phi) - \overline{v}(\phi)] \tag{7}$$

where $\overline{v}(\phi)$ is a second ensemble average and again the ϕ in Reynolds stresses is omitted. For Reynolds shear stresses u_m and v_m are different, but either velocity is repeated for normal stresses.

Table 2 shows the streamwise locations x where SRQ data were acquired at the spanwise center with the associated Gr_x, as well as Re_x and Ri_x at the initial condition. The origin of x was defined at the inlet to the test section that is shown in Fig. 4. External coordinates were used as the boundary layers generally do not meet as in fully-developed pipe flow. Fluid properties were evaluated at the film temperature. Initially buoyancy effects were small, but became dominant at later phases of the transient.

Table 2. Gr_x as well as Re_x and Ri_x at the initial condition and the three locations in x where data were acquired

	x [m]	Gr_x	Re_x $(t=0)$	Ri_x $(t=0)$
x_1	0.16	1.46×10^7	23,300	0.027
x_2	0.78	1.62×10^9	112,000	0.129
x_3	1.39	9.32×10^9	201,000	0.231

2 Experimental Facility

All experiments were performed in the Rotatable Buoyancy Tunnel (RoBuT), which will be described in detail. Benchmark-level validation data were acquired with simple geometry and some multi-physics interaction. The square test section allowed easy characterization using optical velocity measurements. The simple geometry is easy to represent numerically and helps isolate model errors.

2.1 Rotatable Buoyancy Tunnel

The RoBuT is an open-circuit air tunnel with a large 4.81-m diameter 'Ferris wheel' design that allows rotation, thus changing the relative direction of forced flow and buoyant forces without changing the facility. Many important tunnel components are shown in Fig. 4, which is in the buoyancy-opposed orientation used in the current work. Note the coordinate system with the origin on the heated wall at the inlet and the spanwise center. The streamwise distance is x, wall-normal distance is y, and spanwise distance is z with zero along the centerline. The facility rotates on an axis parallel to the z axis around the center of the test section. The laser and cameras were part of a Particle Image Velocimetry (PIV) system that will be described in Sec. 3.2.

The test section had a 0.305×0.305 m square cross section and was 2 m long. It had three clear walls for optical access and a heated wall for a thermal BC. More details of the test section are provided in Sec. 2.2. The contraction and outlet were made of fiberglass-reinforced plastic with a glass-smooth, black gel-coat.

The contraction had an area ratio of 6.25:1 and was 0.914 m long. The contraction bell at the leading edge had a 102 mm radius. Between the contraction and bell were four modular sections that contained—in order of flow direction—a single row, aluminum fin/copper tube, chilled water heat exchanger (Super Radiator Coils Model 30x30-01R-0.625/048); a settling length section; a precision aluminum honeycomb flow straightener; and two high porosity screens. Square turbulence trips 3.175 mm wide were installed along all four walls and located about 0.12 m upstream of the test section inlet.

The outlet expanded the flow downstream of the test section, had a total included angle of 8.2°, and was 0.686 m long. The blower drew air through the test section and ejected it into the room. It included an inline centrifugal fan assembly, TCF/Aerovent model 14-CBD-3767-5. It was belt driven by a 5 HP, TEFC, 230-460 VAC induction motor, Toshiba model B0052FLF2AMH03. The motor was powered by a Toshiba variable frequency drive, model VFS11-2037PM-WN.

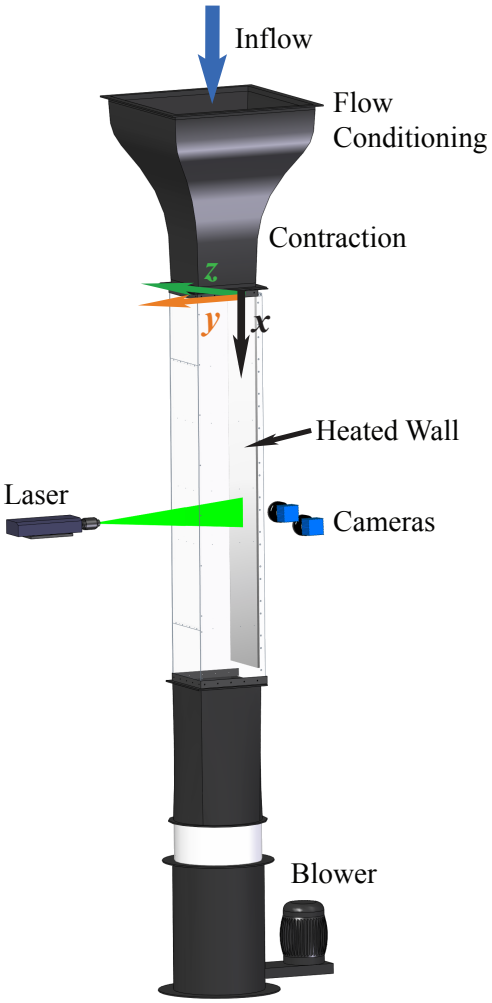

Fig. 4. RoBuT flow components as configured for transient data acquisition

Two Laskin Nozzles [16] were used to atomize olive oil tracer particles. A TSI Aerodynamic Particle Size Spectrometer was used to measure the particles at the outlet; the resulting mean diameter was about 1 µm. These particles were mixed with air and injected into a PVC pipe distribution system upstream of the contraction assembly. A peg board was placed between this system and the beginning of the contraction to aid particle mixing. It had holes 6.35 mm in diameter and were spaced 25.4 mm apart in a square pattern. The volume fraction of oil particles in the air was measured to be about 10^{-9}, so their effect on thermophysical properties can reasonably be neglected.

2.2 Test Section

The test section had four walls, an inlet, and an outlet that will be described in detail. The heated wall, shown in Fig. 5, was a custom design with many layers to provide a heated surface for convection and featured embedded instrumentation. This wall was heated to approximately 130°C for

this study. It was made of three layers of aluminum, had silicon rubber heaters, and contained thermal insulation to drive most of the heat inward. A list of materials and thicknesses is available in Table 3. The surface was nickel plated to reduce thermal radiation, which resulted in a predicted and measured emissivity around 0.03 [2]. Aluminum 2024, though more expensive than the common alloy 6061, was used because its thermal conductivity is known more precisely [17].

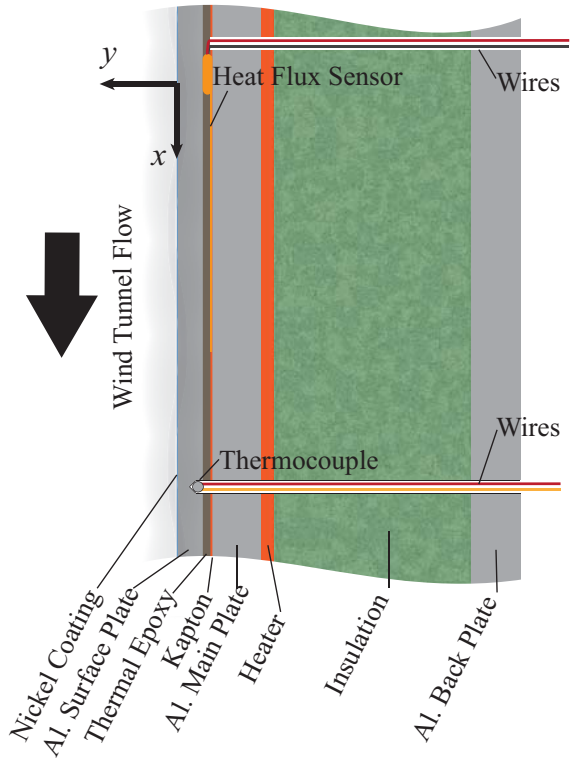

Fig. 5. Heated wall cross section with component names as in Table 3. The relative thicknesses are to scale.

The heated portion was 279 mm wide and 1.89 m long. The left and right sides were thermally insulated by 17.5-mm thick Teflon® that extended into grooves in the side walls for support. Two additional 12.7-mm thick Teflon® insulators were placed upstream and downstream of the heated wall.

There were six heaters, each spanning the width of the heated wall and one sixth of the length. Three HP 6439B power supplies were connected to two heaters each and were used to control the temperature of the wall via a closed-loop PI controller. Three controllers, one for each power supply, allowed the heated wall to be heated in independent sections in the streamwise direction to increase temperature uniformity.

Besides the heated wall, the other three walls were clear Lexan® polycarbonate for optical access and were 12.7 mm thick. From the perspective of standing on the heated wall at the inlet, they are termed left ($z = -152$ mm), top ($y = 305$ mm), and right ($z = 152$ mm) walls. The top wall had a

Table 3. Heated wall components and thicknesses with names from Fig. 5

Name	Material	t [mm]
Nickel Coating	Bright Nickel	∼0.05
Al. Surface Plate	Al. 2024-T3	3.18
Thermal Epoxy	Dow Corning 3-6751	1.02
Kapton®	Kapton® HN Film	0.254
Al. Main Plate	Al. 6061-T651	6.35
Heater	Tempco Silicone Rubber	1.59
Insulation	Mineral Wool	25.4
Al. Back Plate	Al. 6061-T651	6.35

removable center portion for cleaning and maintenance. This wall also had three 25.4-mm ports for probe insertion.

The as-built geometry was measured to account for differences between the as-designed and as-built test section geometries. The differences were small, but the measurements are presented for completeness. An internal micrometer was used to measure the internal dimensions of the fully assembled test section. Height measurements were performed at the left, center, and right as well as width measurements at the top, middle, and bottom. This was done at seven locations in x and performed three times for a measure of random uncertainty. Modelers may use these dimensions when constructing the simulation domain to ensure greater similarity. A sketch of the measurement locations may be accessed from the online database by following the link BC-AsBuiltSketch in the digital version of this work. The nominal values are in BC-AsBuiltMeasurements and uncertainties in BC-AsBuiltMeasurementUncertainties. A Parasolid model created from the as-built measurements is available in BC-AsBuiltGeometry.

A warm-up procedure was followed each time the RoBuT was used for experiments. The HVAC system was kept active at all times for stable room conditions. The heated wall was first heated to the setpoint temperature. Once this was reached, the blower was set to the desired speed for the experiment and the heater controllers would increase power accordingly. Once the temperature was again stable for a minimum of five minutes, the facility was ready for data acquisition. If the blower setpoint speed was changed, the controller would stabilize temperature and the minimum five minute waiting period was repeated.

Between acquiring different series of data, the entire test section was cleaned with Ethyl Alcohol and delicate task wipes to ensure optical quality. The cover on the top wall was removed for inside cleaning. High-vacuum grease was used on test section joints to eliminate air leakage and was removed and reapplied each time a panel of the test section was adjusted.

3 Analog Instrumentation and Signal Processing

Thermocouples were used to measure boundary temperatures, heat flux sensors (HFSs) for heat flux through the heated wall, and PIV for inflow and boundary layer air velocity. Other sensors measured room air conditions. These systems will now be described in detail.

3.1 Thermal Instrumentation

A total of 307 TCs were used to measure boundary temperatures. All test section TCs were 30 gauge Type K from Omega Engineering with Special Limits of Error. They were each welded to length with an Argon-shielded welder. Each TC was calibrated with an Isotherm FASTCAL-M with an accuracy of 0.3°C over a range of 25-190°C with data at every 5°C. Because every TC calibration was very similar and made from the same spool, an average calibration curve was applied. An array of 3×5 TCs, three in y and five in z, was suspended on the downstream side of the honeycomb for inlet air temperature measurements. Each of the three clear walls had 21 TCs with seven rows spaced in x and three across in y for the left and right walls or in z for the top wall. The bulk of the heated wall had 5×32 TCs with five in z and 32 in x. The Teflon® edges each had embedded TCs with five across the leading edge in z and 32 along the sides in x. All TCs were embedded to within 3.18 mm of the inside surface using thermal epoxy with enhanced thermal conductivity.

Three HFSs were embedded into the heated wall along the spanwise center at the x-locations found in Table 2. They were a thin-film type, model 20457-3 from RdF Corporation with a thermopile around a Kapton® substrate. The manufacturer supplied unique calibration coefficients for each sensor. The manufacturer-specified uncertainty was 5% of reading. An embedded Type T TC was used to measure sensor temperature and correct readings with the supplied multiplication factor curve to compensate for changes in thermal conductivity of the substrate. The HFSs were placed adjacent to the Kapton® layer of similar thermal resistance to reduce measurement errors. A thermal resistance network analysis showed only a 2.4% difference in heat flux between HFS and non-HFS conduction paths.

The TC and HFS output voltages were small, so special data acquisition (DAQ) devices were selected. National Instruments (NI) products were used as they interfaced well with the LabVIEW software that was used for system control and thermal data recording. Twenty one NI-9213 TC modules were housed in five NI-cDAQ-9188 chassis. The narrow voltage range of $\pm$78 mV, 24-bit ADC, and open channel detection made them well suited for these measurements. The built-in CJC was used for TCs. The total uncertainty of the calibrated TCs with these DAQs was 1°C, largely due to the CJC uncertainty of 0.8°C. Data from thermal instrumentation were recorded throughout each transient run. Data from thermal instrumentation was recorded through 2400 runs of the transient. These data were ensemble-averaged and the bias, random, and total uncertainties were quantified.

3.2 Particle Image Velocimetry

The PIV system allowed for non-intrusive, full-field velocity measurements at several locations. The system consisted of a laser, cameras, and a timing unit. The laser was a New Wave Research Solo PIV III, a dual cavity, frequency-doubled Nd:Yag model with about 22 mJ/pulse and a wavelength of 532 nm. The cameras were model Imager sCMOS from LaVision and featured a 16-bit sCMOS sensor with 2560×2160 pixels with a pixel size of 6.5 µm. An internal, standard version timing unit was used for the stringent timing requirements of PIV and had a resolution of 10 ns with jitter of $<$1 ns. Two Nikon lenses were used. The first was an AF Nikkor 28 mm f/2.8 D used for the large field of view (FOV) inflow and the large FOV SRQ data that spanned the 0.305-m test section. The second was an AF Micro-Nikkor 105 mm f/2.8 D for high resolution (small FOV) SRQ data near the heated wall.

DaVis 8.2 software was used to acquire and process images. The optical configuration of Fig. 4 was used with the laser sheet normal to the heated wall and camera viewing angles nearly parallel with it. The equipment was moved manually in the x direction. The inflow was measured in the same orientation, but Velmex BiSlide® traverses were used to move the laser and camera consistently in the z direction. In this way, five planes were measured to map the inflow.

PIV calibration was performed in two ways. Because the laser sheet and camera were normal to each other, the inflow used a conventional two-component 'ruler' calibration over a span of about 280 mm. The SRQ data were acquired with two independent two-component cameras, one that spaned the entire test section and one that provided high resolution data near the heated wall. The SRQ data that spanned the test section used a custom two-plane calibration target that filled the image. The SRQ data near the heated wall was calibrated with a single-plane calibration target, model FA119 from Max Levy Autograph, Inc. Both SRQ sets used the pinhole model as the cameras were angled generally less than 8°. This angle was required to avoid image diffraction by the large temperature gradient very near the wall. Because this flow had very little through-plane motion, errors in v velocity from through-plane motion appearing as in-plane motion (a function of the sine of the angle) were expected to be small. The pinhole model was applicable as refraction between the Lexan® and air was small.

Prior to acquisition, the quality of the particle images was checked to ensure proper particle density, diameter, and displacement as well as laser beam overlap and image focus quality. Many of these data parameters and others from the acquired images are found in Table 4. The diameter, density, and displacement were spatially-averaged over the entire image. The maximum displacement was set between 8–32 pixels for all phases of the transient. To optimize dynamic range, two values of dt were used for each PIV acquisition location. Since the reported values are spatially averaged, some may appear different from the ideal simply due to their non-uniformity in space and in time. These data were taken from a phase near the middle of the transient. Both particle diameter and density were determined by methods found in [18]

with the local maximum method for density estimation.

Table 4. PIV data parameters. These are represented with an i/j in the table with the former being used for early phases with larger displacements and the latter for later phases with smaller displacements.

Parameter	Inlet	SRQ-LargeFOV	SRQ-SmallFOV
N image pairs	100/200	100	100
sample frequency [Hz]	5	5	5
dt [µs]	860/3150	385/1541	96/385
lens	28 mm	28 mm	105 mm
extension [mm]	–	–	39.5
calibration [mm/pixel]	0.123	0.121	0.0137
$f\#$	4	4	8
diameter [pixels]	1.98	1.98–2.55	2.68–3.00
density [#/32 × 32]	86.7	57.3–88.1	8.04–11.8
displacement [pixels]	5.35–31.9	1.34–30.3	2.71–29.8

A MATLAB code was written to reorganize images. During acquisition, a set was recorded over all phases of the transient. The code would copy images from all runs for a given phase and create a new set. This process was repeated for all runs so data within each phase could be ensemble-averaged and fluctuations quantified.

The processing of particle images was performed using the muti-pass, multi-grid, window deformation method in DaVis. A mask was carefully defined to remove the influence of walls on the correlation. Round interrogation windows were used for reduced noise. The first two passes were at 128×128 pixels, the next two at 64×64 pixels, and the final four passes at 32×32 pixels. The overlap on every pass was 75%. Vector post-processing was performed where vectors were removed if the peak ratio was less than two. Then a two-pass median filter of 'strongly remove & iteratively replace' corrected spurious vectors. Vectors were removed if their difference from average was more than one standard deviation of neighbors and subsequently replaced if the difference from average was less than two standard deviations of neighbors.

Particle images have the average background removed. Since we have limited use for streamwise information, the pixel range was reduced in the flow direction to 340 pixels for the inflow images and 512 pixels for the SRQ images to reduce storage requirements and processing time. Examples of dewarped particle images with background subtracted are shown in Fig. 6.

3.3 Atmospheric Instrumentation

Air temperature, relative humidity, and atmospheric pressure in the RoBuT room were measured to determine air properties. Both temperature and humidity were measured with an Omega HX93A probe. Pressure was measured with an Apogee Instruments BPS 1006 sensor. The output voltage of these sensors was measured by a NI USB-9215A 4-channel ±10 V analog input DAQ. The uncertainty of temperature was 0.6°C, humidity was 2.5% for readings 20-80% and 3.1% otherwise, and pressure was 3% of reading. These data were sampled at 1 Hz, then averaged and recorded once per minute.

3.4 Uncertainty Quantification

Thermal and atmospheric data uncertainty quantification (UQ) is described here following the methods of Coleman and Steele [19]. UQ for PIV was considered by other methods and is described later. Bias uncertainty parameters were obtained from sensor documentation at the 95% confidence level. The random uncertainty of a general ensemble-average quantity $\bar{x}$ was calculated by

$$S_{\bar{x}} = t_{95}\frac{S_x}{\sqrt{N}} \tag{8}$$

where t_{95} is the confidence level coefficient (taken as 1.96 for 95% confidence and number of samples $N > 30$) and S_x is the sample standard deviation. All samples sizes in this work were large. Bias and random sources are combined as

$$U_{\bar{x}} = \sqrt{B_{\bar{x}}^2 + S_{\bar{x}}^2} \tag{9}$$

where $B_{\bar{x}}$ is the expanded bias uncertainty. The data provided with this paper generally specifies the unique bias, random, and total uncertainty numbers with the ensemble-average results.

Uncertainty of the PIV results was calculated from the Uncertainty Surface Method that estimates instantaneous bias and random uncertainties due to the effects of particle displacement, particle image density, particle image size, and shear. This method was originally described in [20] and improved on with methods from [18]. The uncertainties of the velocity statistics propagated from the instantaneous uncertainties were calculated by the methods of Wilson & Smith [21]. Total uncertainty was calculated as in Eqn. 9. The confidence level on all UQ results in this work is 95%.

4 Boundary Conditions

This section contains a description of all expected requisite BCs for CFD model inputs. The types of BCs were shown in Table 1. The as-built geometry is a BC, but was discussed previously in Sec. 2.2.

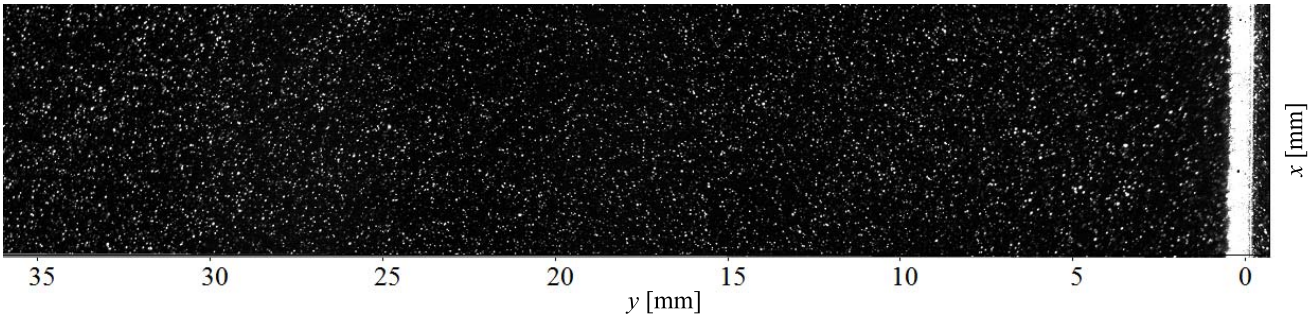

(a) SRQ-Small FOV with heated wall at right

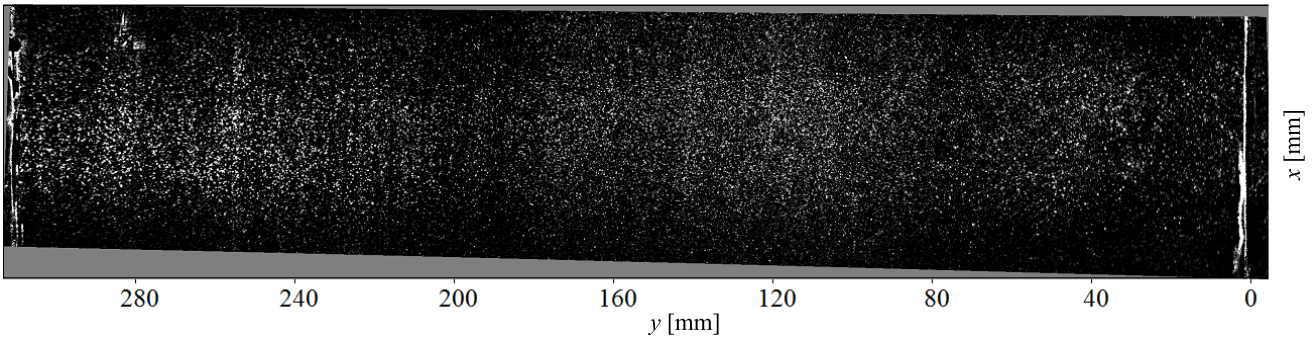

(b) SRQ-Large FOV with heated wall at right and top wall at left

Fig. 6. Dewarped SRQ particle images at x_2 with mean background removed. Note the image scales are about a factor of nine different. Also, the particles to the extreme right are reflections off the heated wall.

4.1 BC Description

The measured BC temperatures are mapped onto the test section geometry in Fig. 7. Note the high measurement resolution on the heated wall and the development of the thermal boundary layer on the right wall as air travels from the inlet to the right of the figure.

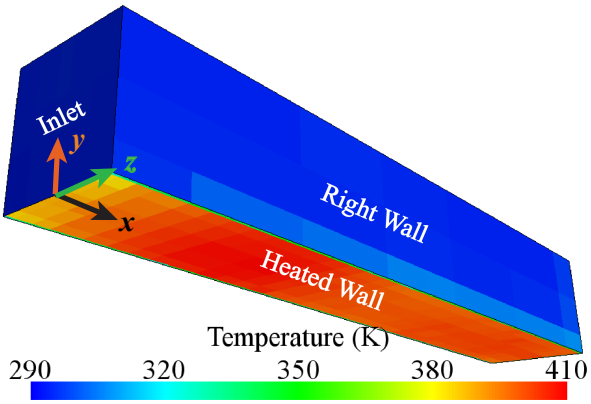

Fig. 7. Measured temperatures on the test section boundaries

As mentioned previously, the inflow was measured in five planes spaced in z with locations concentrated near the side walls. The ensemble-average streamwise velocity $\overline{u}$ at the inlet is shown in Fig. 8 at the initial condition. Gray lines indicate PIV measurement locations that span across y (two are at the left and right edges). Data are highly-resolved in y but not in z. Data may be interpolated from the information given to provide inflow over the entire inlet. Another approach is to use the high-resolution data near the unheated top wall ($y = 305$ mm) boundary layer to the left and right walls, which are also unheated.

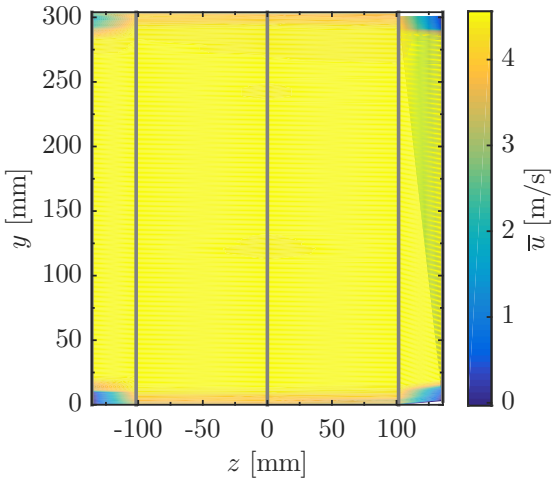

Fig. 8. Measured streamwise velocity $\overline{u}$ at the inlet and the initial condition

The atmospheric conditions include atmospheric pressure, relative humidity, and room temperature and were recorded at the time of data acquisition.

Data acquisition procedures were followed to control

test conditions. The following list describes the steps followed for acquisition of both BC and SRQ data:

1. Begin heating of the heated wall
2. Upon reaching setpoint temperature, start blower
3. Align traverses, laser, and camera with test section at measurement location
4. Align laser sheets
5. Focus camera on particle images
6. Align calibration plane with laser sheet and calibrate camera(s)
7. Determine optimal dt for particle displacement, proper seeding density, and proper laser intensity
8. Record measurement location and other PIV parameters
9. Confirm stability of wall temperature and room conditions
10. Record PIV data, atmospheric and thermal conditions

This process was repeated for PIV measurement locations for the five inflow and the three SRQ data sets. The acquisitions were automated by a LabVIEW program which controlled the conditions, determined when they were stable, initiated the transient and data acquisition (both thermal and PIV), and repeated.

4.2 BC Data

These data are available for all phases of the transient on the inflow and all four walls of the test section. There is one file for each surface that can be found through the following links: BC-InletTemp.csv, BC-HeatedWallTemp.csv, BC-LeftWallTemp.csv, BC-RightWallTemp.csv, and BC-TopWallTemp.csv. The format for all BC files works directly with Star-CCM+ and is easily adaptable to other CFD codes. The columns X, Y, and Z are used throughout this work; adhere to the global coordinates as shown in Fig. 4; and are presented in meters. The column 'T(K)' is the ensemble-average temperature in Kelvin, 'B_T(K)' is the bias uncertainty, 'S_T(K)' is the random uncertainty, and 'U_T(K)' is the total uncertainty. Additionally, time stamps are included for each column header as in 'T(K)[t=0s]', 'T(K)[t=0.2s]' and so forth.

The data file for the inflow ensemble-average and fluctuating velocities is found in BC-Inlet-Vel.csv. Here X, Y, and Z are used as before and are presented in meters. The columns 'u', 'v', and 'w' are ensemble-average velocities in the x, y, and z directions, respectively. The columns 'u′u′', 'v′v′', 'w′w′', and 'u′v′' are specific Reynolds stresses. Uncertainties compose the remaining columns with the uncertainty of $\overline{u}$, $\overline{v}$, and $\overline{w}$. Reynolds stresses have unique plus and minus uncertainties with 'Uuup' being the plus uncertainty of $\overline{u'u'}$ and so on. The units of velocity and velocity uncertainty are [m/s] while those of Reynolds stresses and their uncertainties are [m^2/s^2]. Again, time stamps are included in column headers.

Note that inflow out-of-plane velocities $\overline{w}$ and $\overline{w'w'}$ were assumed to be the same as $\overline{v}$ and $\overline{v'v'}$ respectively. This assumption was proved valid in previous work in this facility by measuring the inflow in both directions with two-component PIV and comparing data where measurement planes intersect [2]. The atmospheric measurements, together with their uncertainties, are found in the file BC-AtmCond.csv.

5 Fluid and Material Properties

As air was the working fluid, measurements of temperature, pressure, and relative humidity discussed in Sec. 4.2 were sufficient to define all fluid properties. It is important to note that the working pressure is different from that at sea level as the experiment was conducted in Logan, Utah at 1460 meters above sea level.

Material properties of the test section can be obtained from the information provided in Sec. 2.2. It may not be necessary to include the heated wall in the model since temperature measurements were made very near the surface, but the information is provided for completeness. On the other hand, a simulation without the thermal capacitance of this wall may predict an unnaturally high sensitivity to local convection conditions.

6 Test Conditions

For improved statistics, the data were ensemble-averaged over repeated runs. A total of 2400 runs were used, with 100-200 for each PIV acquisition location and dt. Steady thermal conditions triggered data acquisitions and simultaneously cut power to the blower, initiating transient conditions. Heater power was fixed through each run.

LabView was used to control test conditions and to acquire thermal data via a NI DAQ system. This system created a master TTL signal used for clocks in both the thermal and PIV equipment for synchronized thermal and velocity data acquisition. Data were acquired at 5 Hz for a period of 20.2 s.

The RoBuT room was configured with modern HVAC systems and thermal insulation for stable conditions. Controls were independent of other systems in the building. The refrigerated air conditioning had a $\sim 0.56°C$ (1°F) deadband. To reduce the rate of temperature change from the on/off behavior of this system, outside air was mixed with refrigerated air before being injected into the room. The maximum measured temperature spread during data acquisition was 0.9°C ($\sim$ 1.6°F). Heating was performed with a steam heat exchanger with attached fan. The original fan and control system were replaced with a variable speed, tuned, PI-controlled system implemented with the main LabVIEW program, giving the heating system tight control of room temperature.

7 System Response Quantities

The SRQs are the experimental results used to compare with simulation outputs and were listed in Table 1. They are included for all phases of the transient and include uncertainty on all results. Since they are similar, the ensemble-average and fluctuating velocity profiles in the

form of Reynolds stresses are presented together. Additionally, scalars of wall heat flux and wall shear stress are included.

7.1 SRQ Description

Profiles of streamwise velocity $\overline{u}$ and Reynolds normal stress $\overline{u'u'}$ are shown in Figs. 9 & 10 respectively at three locations in x for the top (x_1), middle (x_2), and bottom (x_3). The boundary layer thickness increases in the streamwise direction x as evidenced in both the $\overline{u}$ and $\overline{u'u'}$ profiles at the initial condition as expected. The velocity profile shape generally remains similar, but is reduced in magnitude during the first four seconds. The effects of natural convection become visible at $t = 8$ s near the heated wall ($y = 0$). At $t = 12$ s the profiles show a strong influence from natural convection. The changes from $t = 12 - 16$ s are subtle as steady natural convection is asymptotically reached.

The results for Reynolds normal stress $\overline{u'u'}$ show larger uncertainty, but this is expected as fluctuations are more challenging to quantify than averages [22]. Initially $\overline{u'u'}$ is elevated near both walls as expected. The influence of natural convection increases $\overline{u'u'}$ near the heated wall initially. The area of elevated $\overline{u'u'}$ moves away from the wall over time. The highest levels occur at $t = 12$ s, likely from a chaotic flow reversal. The final measured state has reduced stresses that may still be decreasing.

Previous methods to quantify wall shear have fit experimental velocity data with empirical correlations such as Spalding or Musker profiles with high accuracy [23]. This method works well for steady boundary layer data where these two profiles are an accurate representation of velocity, but not for the transient conditions in the current study. Therefore, wall shear stress was estimated directly from PIV data as $\tau_s = \mu \frac{\partial \overline{u}}{\partial y}\big|_{y=0}$ where τ_s is wall shear stress and μ is dynamic viscosity. High-resolution PIV data were used to fit a line to velocity data within the range $y^+ = y u_\tau / \nu \leq 5$ for the velocity gradient at the wall $\frac{\partial \overline{u}}{\partial y}\big|_{y=0}$, where $u_\tau = \sqrt{\tau_s/\rho}$ and ρ is the fluid density [15].

Initially 10 points were included in the fit and a stable iterative method was used to calculate τ_s and the number of data points to fit within $y^+ \leq 5$. The wall was located by the particle images with a mask carefully defined. The linear fit was performed using linear regression with more weight given to velocity data with lower uncertainty [24]. The high-resolution PIV data at x_2 and associated linear fit are shown in Fig. 11 for five phases of the transient. The fit was not forced to the wall for two reasons: 1) the wall location determined by the image has unknown errors and 2) these unknown errors cannot be propagated in the uncertainty estimation. The dynamic viscosity was evaluated using Sutherland's Law at the wall temperature. The fit uncertainty was combined with the viscosity uncertainty using the Taylor Series Method [19].

Results for the scalars of wall heat flux and wall shear stress are shown in Figs. 12 & 13 respectively at the three x locations and through time with their associated uncertainty bands. The experimental heat flux was measured with

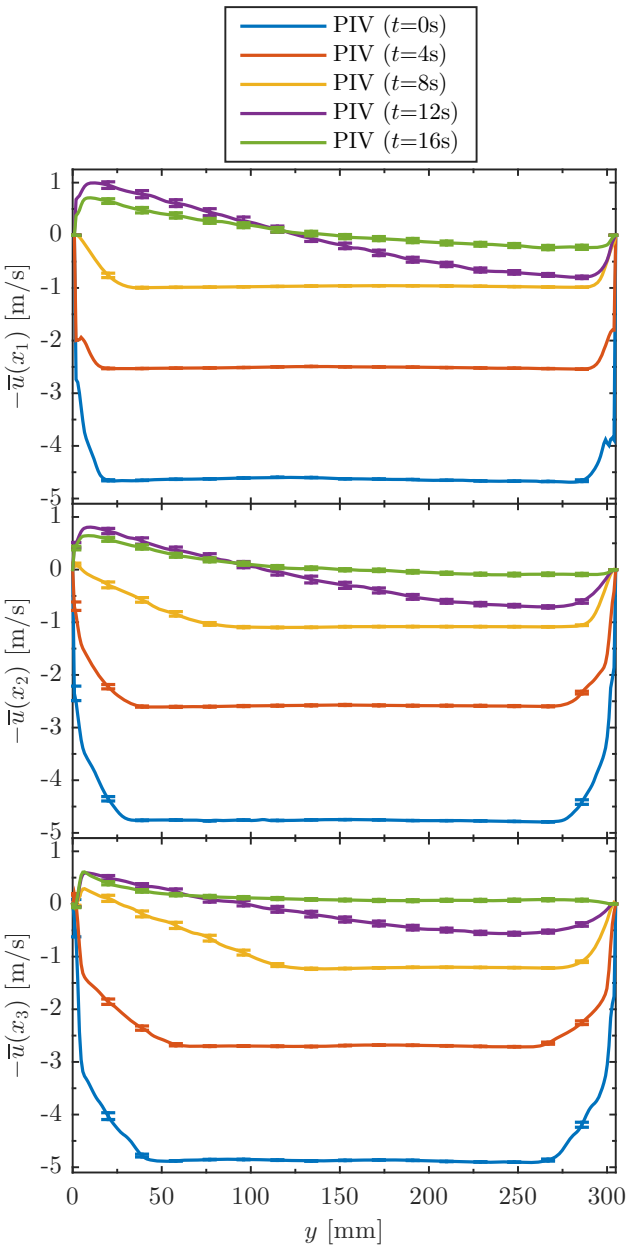

Fig. 9. The streamwise velocity $\overline{u}$ at three locations in x and five phases of the transient

HFSs using the manufacturer-calibrated sensitivity. The uncertainty included 5% bias while the random uncertainties are based on the standard deviation of the measurements. The experimental results from the HFSs show a low sensitivity to convection due to the thermal capacitance of the heated wall in which they were embedded.

The wall shear results are somewhat noisy at high levels of shear, likely from the decreased accuracy of PIV data near walls with large velocity gradients and the relatively lower number of points in the fit. When shear decreases, so does the velocity gradient and more points can be used in the fit for smoother results with decreased uncertainty. The shear also changes sign smoothly as the near-wall flow reverses.

In the work by He and Jackson [7], several parameters

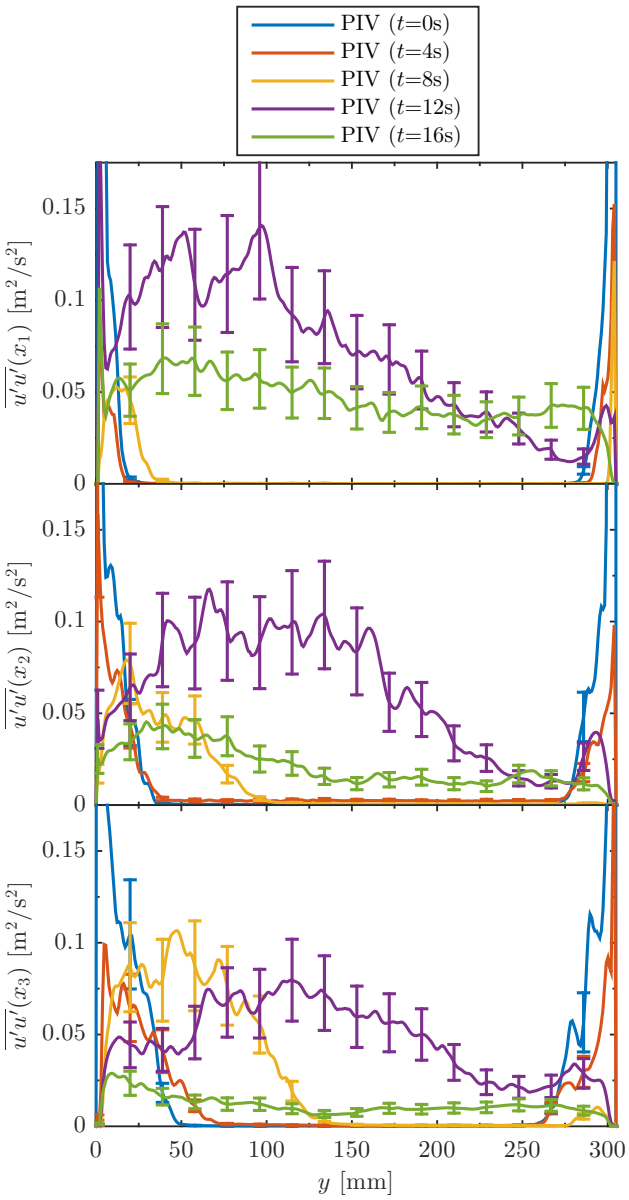

Fig. 10. Reynolds normal stress $\overline{u'u'}$ at three locations in x and five phases of the transient

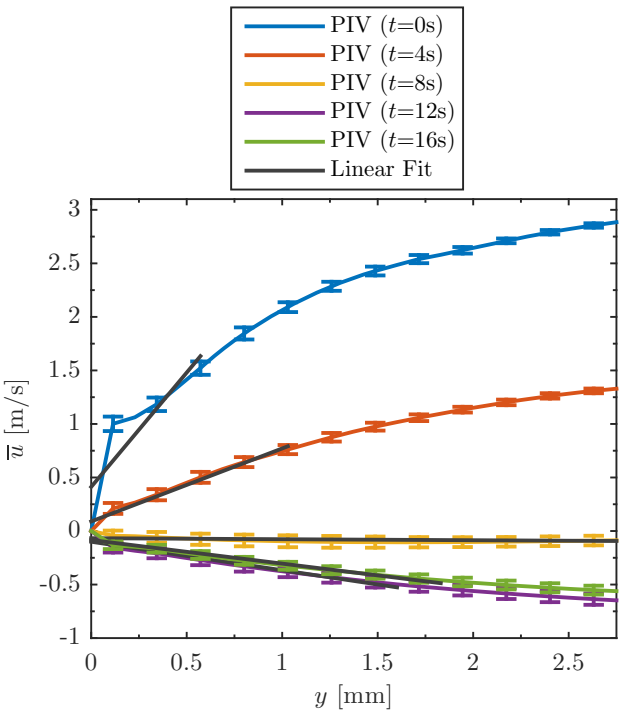

Fig. 11. High-resolution PIV data near the heated wall with linear fit that extends from the wall to the last data point with $y^+ \leq 5$

were presented to estimate the degree to which transient behavior should depart from that of pseudo-steady flow, meaning an unsteady flow that is similar to steady flow at the same instantaneous Reynolds number. They claimed three non-dimensional parameters can be used to scale ramp-type transient flows: the initial Reynolds number Re_1, the final Reynolds number Re_2, and a ramp rate parameter α. These parameters were defined for fully-developed flow in a pipe without buoyancy effects, but in this work they were estimated using the hydraulic diameter of the test section. He and Jackson manipulated these parameters to give another form of the ramp rate parameter as

$$\gamma = \frac{D}{u_{\tau,0}} \left(\frac{1}{\overline{u}_{\mathrm{bulk},0}} \frac{\mathrm{d}\overline{u}_{\mathrm{bulk}}}{\mathrm{d}t} \right) \tag{10}$$

where D is pipe diameter, $u_{\tau,0}$ is the initial friction velocity, and $\overline{u}_{\mathrm{bulk},0}$ is the initial bulk velocity. Absolute values of γ far below unity are expected to be pseudo-steady while those greater than unity are expected to exhibit notable evidence of transient behavior. The values for the parameters in this study are shown in Table 5 and suggest the flow may be somewhat pseudo-steady as the magnitude of γ is in a gray area. Note that the final Reynolds number Re_2 is in the opposite direction to the initial based on the sign change of bulk velocity shown in Fig. 3. To estimate $\mathrm{d}\overline{u}_{\mathrm{bulk}}/\mathrm{d}t$, a line was fit to the bulk velocity curve from the initial condition until the sign change. Instantaneous values of γ were also estimated. The minimum and maximum values of instantaneous γ were -0.237 and 0.013 respectively. The minimum value suggests the flow transient may have an influence on results. This is supported by the comparison of velocity results presented in the next paragraph.

Table 5. Transient flow parameters used in this study

Re_1	Re_2	α	γ
63,900	2,610	-2.46×10^7	-0.149

To assess any departure from pseudo-steady results, a comparison is made between a steady case that was described in the work of Lance *et al.* [**?**] in the same facility with the same orientation using a phase with similar inlet bulk velocity at $t = 3.6$ s. The streamwise velocity $\overline{u}$ is shown in

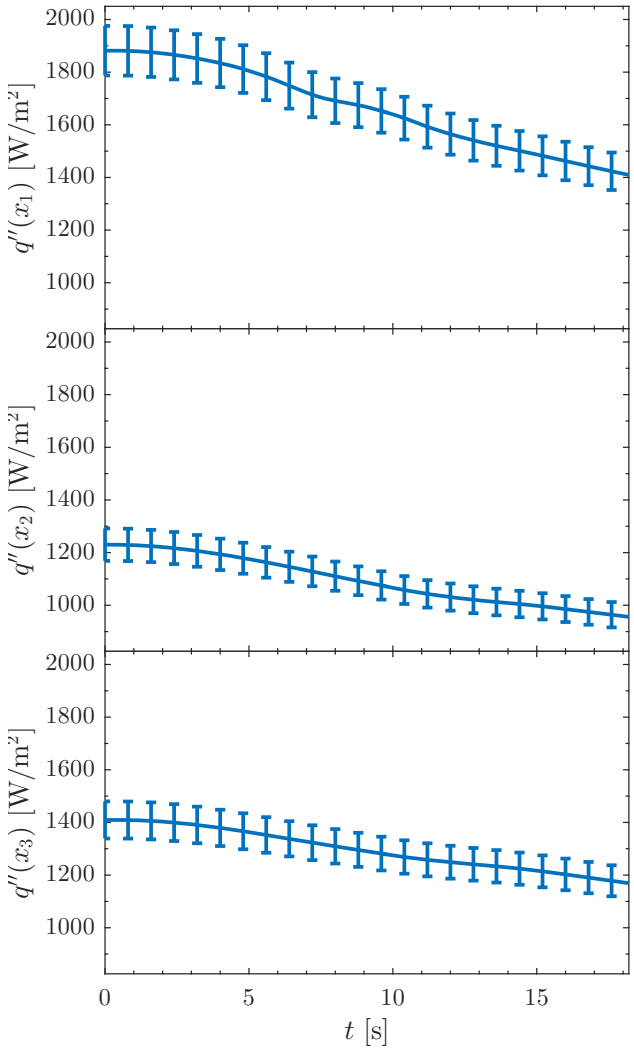

Fig. 12. The heated wall heat flux plotted through time

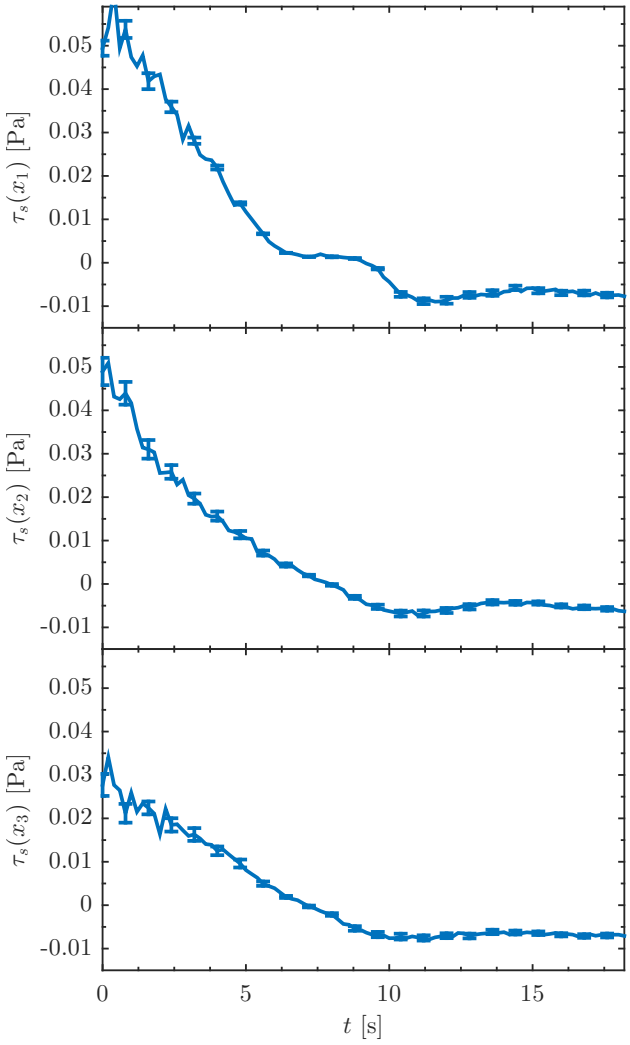

Fig. 13. The heated wall shear stress plotted through time

Fig. 14 and shows only small differences except at x_1, where the transient results show much higher wall shear and consequently high momentum in the boundary layer. The streamwise Reynolds stress $\overline{u'u'}$ is shown in Fig. 15 and again shows a high level of similarity, except at x_1, where the turbulence levels in the transient case are elevated very near the wall and decreased away from the wall. The uncertainty bands for the transient case are larger in both results, mostly due to the higher random uncertainty from only having 100 runs to ensemble-average in this phase compared to the 1000 image pairs in the steady case. Nevertheless, the uncertainty bands generally overlap. The transient profiles show notable departure at x_1 but are otherwise similar.

7.2 SRQ Data

Like the BC data, the SRQ data and their uncertainties are tabulated for use in validation studies. They are contained in comma separated files with the *.csv extension and can be opened in a spreadsheet program or a simple text editor. All resulting PIV data are made available from both cameras with headers similar to the BC PIV data presented earlier. They contain data at all three x locations as specified in the files. As with the BC data, the full uncertainties at 95% confidence are provided with unique positive and negative uncertainties for Reynolds stresses. The small FOV data are found in the file SRQ-Vel-SmallFOV.csv and the large FOV in SRQ-Vel-LargeFOV.csv. Wall heat flux results are given for all three sensors along x with specified bias, random, and total uncertainty and found in the file SRQ-HeatFlux.csv. Wall shear is similarly formatted, has the total uncertainty, and is found in the file SRQ-Shear.csv.

8 Conclusions

This paper presented the study of a ramp-down flow transient with heat transfer and buoyancy effects in simplified geometry to provide CFD validation benchmark data. Repeated runs provided high-resolution data for ensemble-averaging and turbulent statistics of high resolution data. The provided BCs and SRQs, listed in Table 1 for the conditions in Table 2, are tabulated and available for download. Uncertainties are also included for all presented data. The data

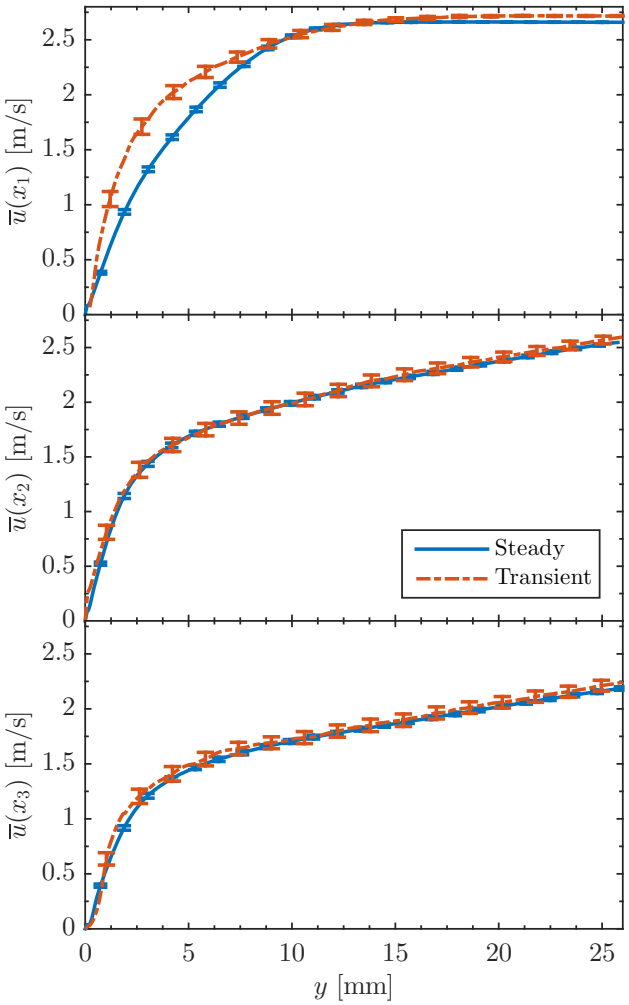

Fig. 14. Streamwise velocity $\overline{u}$ comparison between a steady case and the phase at $t = 3.6$ s with matched inlet bulk velocity at all three locations in x

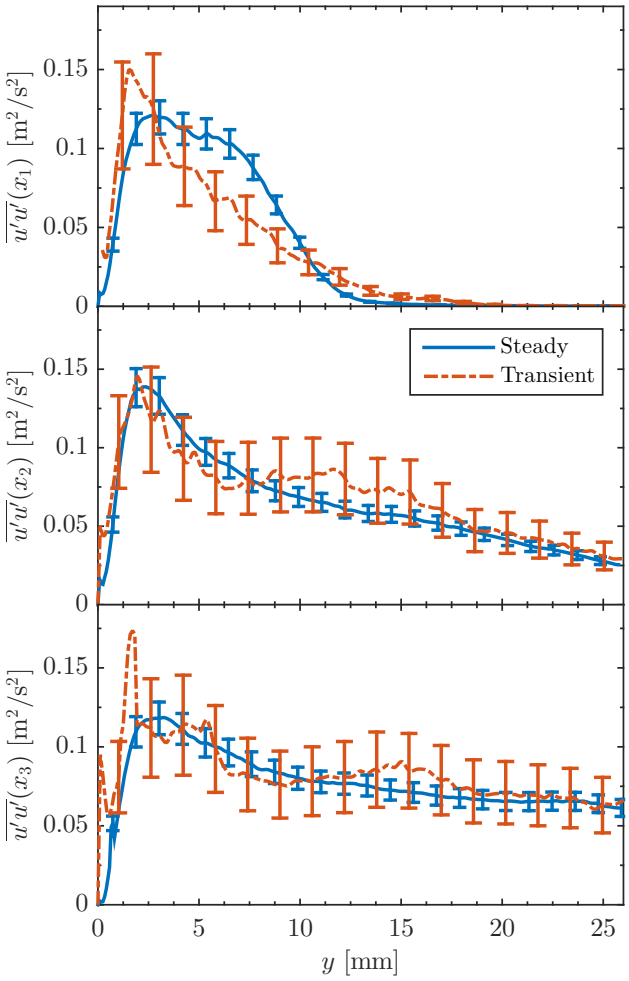

Fig. 15. Streamwise Reynolds stress $\overline{u'u'}$ comparison between a steady case and the phase at $t = 3.6$ s with matched inlet bulk velocity at all three locations in x

contain rich and comprehensive coverage of this flow. They enable validation studies to assess model accuracy and are necessary to calculate model form uncertainty.

Acknowledgements

This research was performed using funding received from the DOE Office of Nuclear Energy's Nuclear Energy University Programs. Their support is gratefully acknowledged. Also, the authors appreciate Dr. Nam Dinh, who originally suggested transient convection for CFD validation.

References

[1] Oberkampf, W. L., and Smith, B. L., 2014, "Assessment Criteria for Computational Fluid Dynamics Validation Benchmark Experiments," 52nd Aerospace Sciences Meeting of AIAA.

[2] Harris, J. R., Lance, B. W., and Smith, B. L., 2016, "Experimental Validation Data for CFD of Forced Convection on a Vertical Flat Plate," *J. Fluids Eng.*, **138**(1), p. 011401, doi:10.1115/1.4031007.

[3] Lance, B. W., Harris, J. R., and Smith, B. L., 2016, "Experimental Validation Benchmark Data for CFD of Mixed Convection on a Vertical Flat Plate," *J. of Verification, Validation and Uncertainty Quantification*, doi:10.1115/1.4032499.

[4] Oberkampf, W. L., and Roy, C. J., 2010, *Verification and Validation in Scientific Computing*, Cambridge University Press.

[5] ASME, 2009, "ASME V&V 20-2009: Standard for Verification and Validation in Computational Fluid Dynamics and Heat Transfer," Standard, American Society of Mechanical Engineers.

[6] AIAA, 1998, "Guide for the Verification and Validation of Computational Fluid Dynamics Simulations," Tech. Rep. AIAA G-077-1998, American Institute or Aeronautics and Astronautics, Reston, VA, doi:10.2514/4.472855.

[7] He, S., and Jackson, J. D., 2000, "A Study of Turbulence Under Conditions of Transient Flow in a

Pipe," *Journal of Fluid Mechanics*, **408**, pp. 1–38, doi:10.1017/s0022112099007016.

[8] Hino, M., Kashiwayanagi, M., Nakayama, A., and Hara, T., 1983, "Experiments on the Turbulence Statistics and the Structure of a Reciprocating Oscillatory Flow," *J. Fluid Mech.*, **131**, pp. 363–400, doi:10.1017/s0022112083001378.

[9] Koshkin, V., Kalinin, E., Dreitser, G., Galitseisky, B., and Izosimov, V., 1970, "Experimental Study of Nonsteady Convective Heat Transfer in Tubes," *International Journal of Heat and Mass Transfer*, **13**(8), pp. 1271–1281, doi:10.1016/0017-9310(70)90068-2.

[10] Kataoka, K., Kawabata, T., and Miki, K., 1975, "The Start-up Response of Pipe Flow to a Step Change in Flow Rate," *Journal of Chemical Engineering of Japan*, **8**(4), pp. 266–271, doi:10.1252/jcej.8.266.

[11] Maruyama, T., Kuribayashi, T., and Mizushina, T., 1976, "The Structure of the Turbulence in Transient Pipe Flows," *Journal of Chemical Engineering of Japan*, **9**(6), pp. 431–439, doi:10.1252/jcej.9.431.

[12] Rouai, N. M., 1987, "Influence of Buoyancy and Flow Transients on Turbulent Convective Heat Transfer in a Tube," Ph.D. thesis, University of Manchester, UK.

[13] Jackson, J. D., Büyükalaca, O., and He, S., 1999, "Heat Transfer in a Pipe Under Conditions of Transient Turbulent Flow," *International Journal of Heat and Fluid Flow*, **20**(2), pp. 115–127, doi:10.1016/s0142-727x(98)10056-5.

[14] Barker, A. R., and Williams, J. E. F., 2000, "Transient Measurements of the Heat Transfer Coefficient in Unsteady, Turbulent Pipe Flow," *International Journal of Heat and Mass Transfer*, **43**(17), pp. 3197–3207, doi:10.1016/s0017-9310(99)00305-1.

[15] Kays, W. M., Crawford, M. E., and Weigand, B., 2012, *Convective Heat and Mass Transfer*, McGraw-Hill.

[16] Kähler, C. J., Sammler, B., and Kompenhans, J., 2002, "Generation and Control of Tracer Particles for Optical Flow Investigations in Air," *Experiments in Fluids*, **33**, pp. 736–742, doi:10.1007/s00348-002-0492-x.

[17] Touloukian, Y. S., and Ho, C. Y., 1977, *Thermophysical Properties of Selected Aerospace Materials Part II: Thermophysical Properties of Seven Materials*, Purdue University, West Lafayette.

[18] Warner, S. O., and Smith, B. L., 2014, "Autocorrelation-based estimate of particle image density for diffraction limited particle images," *Measurement Science and Technology*, **25**(6), p. 065201.

[19] Coleman, H. W., and Steele, W. G., 2009, *Experimentation, Validation, and Uncertainty Analysis for Engineers*, John Wiley & Sons, doi:10.1002/9780470485682.

[20] Timmins, B. H., Wilson, B. W., Smith, B. L., and Vlachos, P. P., 2012, "A Method for Automatic Estimation of Instantaneous Local Uncertainty in Particle Image Velocimetry Measurements," *Experiments in Fluids*, **53**(4), pp. 1133–1147, doi:10.1007/s00348-012-1341-1.

[21] Wilson, B. M., and Smith, B. L., 2013, "Taylor-series and Monte-Carlo-method Uncertainty Estimation of the Width of a Probability Distribution Based on Varying Bias and Random Error," *Meas. Sci. Technol.*, **24**(3), p. 035301, doi:10.1088/0957-0233/24/3/035301.

[22] Wilson, B. M., and Smith, B. L., 2013, "Uncertainty on PIV mean and fluctuating velocity due to bias and random errors," *Measurement Science and Technology*, **24**(3), p. 035302.

[23] Kendall, A., and Koochesfahani, M., 2007, "A Method for Estimating Wall Friction in Turbulent Wall-bounded Flows," *Exp Fluids*, **44**(5), pp. 773–780, doi:10.1007/s00348-007-0433-9.

[24] Bevington, P. R., and Robinson, D. K., 2003, *Data Reduction and Error Analysis*, McGraw–Hill, New York.

List of Figures

List of Tables